On the Role of Topography in the Ocean Circulation: Diffusive and Inertial Effects

PAOLA CESSI*

MIT–WHOI Joint Program in Physical Oceanography, Massachusetts Institute of Technology, Cambridge, Massachusetts

9 December 1987 and 29 November 1988

ABSTRACT

In an earlier paper it was shown that the presence of bottom topography can substantially alter the Sverdrup prediction for the large-scale wind driven flow. In their model the abyssal water is set in motion by the eddy field, parameterized as lateral diffusion of potential vorticity. If the topography has a structure in the east-west direction, then the solution found in the inviscid limit by Cessi and Pedlosky predicts the occurrence of strong jets in the interior of the model ocean. In this note I used a numerical model to test whether the jets predicted by the analytic solutions survive when inertia and diffusion are included explicitly.

In the inviscid limit, according to the structure of the topography these internal jets can occur in both vertically homogeneous and stratified models. Specifically, if the topographic slope changes sign, then one kind of jets is observed both in baroclinic and barotropic models. In the present work it is shown that this phenomenon is observed with moderate amounts of diffusion and is not disturbed by the occurrence of recirculating inertial gyres within the basin.

If the topographic slope is constant, then another kind of internal jets is theoretically predicted in the inviscid limit, and it occurs in stratified models only. Numerical calculations did not exhibit this kind of internal jets in the presence of inertia and weak diffusion, and the reasons for this failure are rationalized.

1. Introduction

In a previous work Cessi and Pedlosky (1986, hereafter referred as CP) have analyzed what happens when the large scale wind-driven circulation reaches the ocean floor, where topographic relief is present. In that work, the abyssal waters are set in motion by weak vertical transfer of horizontal momentum, from the wind-forced surface waters to the bottom. If the interface stress due to the eddy field is weak, then the abyssal flow is substantial only in regions where the geostrophic contours are closed (see Rhines and Young 1982). In the limit of infinitesimal diffusion the abyssal flow outside the closed geostrophic contours is zero. In the presence of bottom relief which depends on longitude, this leads to a mismatch of the flow along some portion of the abyssal flow boundary, and this is a region which is typically in the basin interior. The reason why the circulation inside the closed geostrophic contours cannot be closed without appending boundary layers is very similar to the mechanism that produces western boundary layers in a closed basin. In the presence of x-dependent topography, closed geostrophic contours occur in a region where the total input of vorticity, injected at the surface by the wind and transmitted downward by the interface stress, is nonzero. Therefore the abyssal circulation, which has to be contained within the closed geostrophic contours in the inviscid limit, cannot be closed without appending diffusive boundary layers. Cessi and Pedlosky show that the flow mismatch arises regardless of the detailed processes which force the abyssal waters, as long as such forcing is weak, and provided that the topography is x-dependent. Although the internal boundary layers can occur both in the abyssal and in the surface waters, this is a phenomenon which occurs only in baroclinic models.

Internal jets can be produced also by a different mechanism if the topographic slope changes sign. Because this phenomenon does not rely on the baroclinicity of the flow, its nature will be explained using a vertically homogenous model. In the presence of topography and planetary vorticity, the large-scale geostrophic contours for a homogenous flow are simply given by $\beta y + f_0 h_b/H$ where h_b is the bottom relief. The free, unforced flow will be along the geostrophic contours. If the topographic slope changes sign then there will be some geostrophic contours which are close together in the interior, but that trace back to regions on the basin boundaries that are far apart (for example, see the contours -0.2 and -0.3 in Fig. 1b). In general the wind forcing imparted in regions that are far apart will be of different strength. The free component of the flow (the one along the geostrophic contours) induced on the basin boundary by the wind forcing, will be thus very different for geostrophic contours that are

* Present affiliation: Scripps Institution of Oceanography.

Corresponding author address: Dr. Paola Cessi, Scripps Institute of Technology, University of California at San Diego, Mail Code A-021, La Jolla, CA 92093.

far apart on the boundary. Since such free flow component is conserved along the geostrophic contours, in the region where the geostrophic contours get closer, the flow will develop a discontinuity. This phenomenon has been qualitatively discussed by Welander (1969) in the context of flow around islands, driven by uniform upwelling. In summary, CP showed that, in the presence of x-dependent topography, internal jets arise when Sverdrup dynamics are used.

It is not obvious a priori that all the assumptions made in CP about the higher order effects will hold when, for example, diffusion is explicitly introduced in the calculations. It is also conceivable that, when relative vorticity is retained, the internal jets will become unstable, violating the assumption that the solutions found in CP represent possible mean fields. Thus, in order to test whether the internal jets described in CP can be observed in the presence of small diffusion and inertia, both relative vorticity and diffusive terms will be explicitly included in the calculations developed in the present work.

A special comment should be made about the role of relative vorticity. Ierley and Young (1983) have shown that, in the absence of relative vorticity, frictional western boundary layer dynamics can affect the interior flow. In their calculation, because all the flow lines go through a frictional western boundary current, the homogenization arguments of Rhines and Young (1982) do not apply, and the relation between the streamfunction and the potential vorticity in the interior of the unforced layers is not simple.

In the analysis presented in Ierley and Young (1983), the western boundary viscous dynamics play an essential role in the region where the boundary current separates (the northwest corner in the subtropical gyre). In models that include relative vorticity, such as that of Holland et al. (1984), a recirculating gyre is established in the region where the boundary current leaves the coast, and many of the interior streamlines pass through the northern boundary layer sandwiched between the recirculating gyre and the zero wind-stress curl line (for example, see Fig. 6 in this paper), invalidating the arguments presented in Ierley and Young (1983). For reasons that are yet unclear, the occurrence of the recirculating gyre favors homogenization of potential vorticity in the unforced layers.

2. Numerical experiments

The inclusion of relative vorticity and of weak, but finite diffusion makes the problem analyzed in CP analytically untractable. Solutions were found by means of a numerical model developed by Ierley. A brief description of the model is given in appendix A. Here, I will just mention that Ierley's model is a low resolution model (not eddy resolving), which, being a spectral model, concentrates most of the resolution at the solid boundaries. The numerical model solves the quasi-geostrophic equations

$$\frac{\partial q_1}{\partial t} + J(\psi_1, q_1) = f_0 w_e / H_1 + \kappa \nabla^2 q_1$$

$$\frac{\partial q_2}{\partial t} + J(\psi_2, q_2) = -\delta \nabla^2 \psi_2 + \kappa \nabla^2 q_2 \qquad (2.1)$$

where

$$q_1 = \nabla^2 \psi_1 + F_1^* (\psi_2 - \psi_1) + \beta y$$

$$q_2 = \nabla^2 \psi_2 + F_2^* (\psi_1 - \psi_2) + \beta y + f_0 h_b b(x, y)/H_2$$

with boundary conditions $\psi_1 = \psi_2 = \nabla^2 \psi_1 = \nabla^2 \psi_2 = 0$ on $x = \pm L_x$, $y = \pm L_y$; $w_e = wg(x, y)$ is the Ekman pumping applied at the top of the upper layer, κ is the coefficient of lateral diffusion of potential vorticity, δ is the coefficient of bottom friction, $F_1^* = f_0^2/(g'H_1)$ is the inverse of the squared Rossby radius of deformation, $F_2^* = F_1^* H_1/H_2$, and h_b is a typical height of the bottom elevation while $b(x, y)$ is the form of the topography. There are thus six dimensional external parameters that determine the solution. Numerical solutions are more conveniently found when (2.1) is put in nondimensional form with the choice

$$(x, y) = L_y(x'/\epsilon, y') \quad \epsilon = L_y/L_x$$

$$\psi_n = \frac{L_y f_0 w}{\epsilon \beta H_1} \psi_n'$$

$$t = \frac{\beta L_y H_1}{f_0 w} t'$$

$$q_n = \beta L_y q_n'$$

$$\kappa = \frac{f_0 w L_y}{\beta H_1} \kappa'$$

$$\delta = \epsilon \beta L_y \delta'.$$

Dropping the primes, (2.1) becomes

$$\frac{\partial q_1}{\partial t} + J(\psi_1, q_1) = g(x, y) + \kappa \nabla^2 q_1$$

$$\frac{\partial q_2}{\partial t} + J(\psi_2, q_2) = -\delta \nabla^2 \psi_2 + \kappa \nabla^2 q_2 \qquad (2.2)$$

where

$$q_1 = \gamma \nabla^2 \psi_1 + F_1(\psi_2 - \psi_1) + y$$

$$q_2 = \gamma \nabla^2 \psi_2 + F_2(\psi_1 - \psi_2) + y + hb(x, y)$$

$$\nabla^2 = \frac{\partial^2}{\partial y^2} + \epsilon^2 \frac{\partial^2}{\partial x^2}$$

with boundary conditions $\psi_1 = \psi_2 = \nabla^2 \psi_1 = \nabla^2 \psi_2 = 0$ on $x = \pm 1$, $y = \pm 1$. All the quantities are now nondimensional. If a velocity scale is defined as $U = f_0 w/(\epsilon \beta H_1)$ then $\gamma = U/(\beta L_y^2)$ is the square of the ratio of the inertial boundary layer thickness to the north–south basin scale, $F_n = F_n^* \epsilon U/\beta$ is the square of the

ratio of the inertial scale to the Rossby deformation radius. Here $h = f_0 h_b/(\beta L_y H_2)$ is the ratio of the topographic effect to the planetary vorticity gradient, κ is now the inverse of the Reynolds number and δ is the ratio of the Stommel boundary layer width to the basin scale.

Here the diffusive term $\kappa\nabla^2 q$ is intended as a parameterization of the effect of the transient eddies on the mean, time averaged, large scale circulation. The main motivation for the choice made here comes from results from eddy resolving models (Holland et al. 1984) which show that, once the transient component of the circulation is averaged out, the time mean circulation in the unforced layers occur in a region where potential vorticity is homogenized. Indeed, as Rhines and Young (1982) have shown, homogenization in the unforced layer is achieved in the steady state if the diffusive term is in the form $\kappa\nabla^2 q_2$. Because all the calculations in CP have been done under the assumption that potential vorticity is constant in the lower layer it would be desirable to be able to compare the inviscid results with those obtained using finite diffusion. The choice of $\kappa\nabla^2 q_2$ as a parameterization of the transient eddies (not resolved by the model used here) achieves this purpose.

Since the goal of this work is to study some processes rather than to simulate realistic oceanic features, the values used for the parameters should reflect their order of magnitude only. With this in mind typical choices are $L_y = L_x = 1000$ km, $g' = 0.01$ m s^{-2}, $\beta = 10^{-11}$ m^{-1} s^{-1}, $f_0 = 10^{-4}$ s^{-1}, $H_1 = H_2 = 1000$ m, $\kappa_{dim} = 100$ m^2 s^{-1}, $\delta_{dim} = 10^{-7}$ s^{-1}, $w = 10^{-4}$ cm s^{-1}, $h_b = 100$ m. This gives, for the nondimensional parameters, the following order of magnitudes:

$$\gamma = 10^{-3}$$
$$F_n = 1$$
$$\kappa = 10^{-2}$$
$$\delta = 10^{-2}$$
$$h = 1.$$

For the values just quoted the nondimensional inertial boundary layer thickness $\gamma^{1/2} \approx 0.03$ while the Munk layer thickness is $(\kappa\gamma)^{1/3} \approx 0.02$. Thus the boundary layer thicknesses are of the same order and the western boundary dynamics are fully nonlinear. For a boundary layer thickness of 0.02, the model at hand has the equivalent of four grid points in the boundary layer. Although four grid points would be insufficient in a finite difference model, in a spectral model, where all the derivatives are computed exactly, the abovementioned resolution is sufficient.

The numerical values of the nondimensional parameters actually used in the experiments were chosen in such a way as to be as close as possible to the inviscid cases analyzed in CP, given the constraints of the low resolution of the model. The purpose of the numerical experiments is to observe the occurrence of the internal jets described in CP, in the presence of small diffusive processes and of relative vorticity. In the following I will describe the results obtained.

3. Ridge-like topography

In the presence of a topography of varying slope, the main result found by CP was that an internal boundary layer connects the western boundary layer to the topographically induced southern boundary layer. In the inviscid limit the internal boundary layer appeared as a discontinuity in transport due to the change in sign of the bottom topography and it was found in both baroclinic and barotropic models.

Specifically, in a two-layer model it was found that, in the absence of relative vorticity and of bottom friction, and with the assumption that $q_2 = $ const. in the region of abyssal flow, the transport across the discontinuity was the same in both layers and therefore there was no jump in potential vorticity.

Three experiments will be discussed. All of them have an Ekman pumping of the form $g(x, y) = -\cos(\pi y/2)$ and the bottom topography has the form $hb(x, y) = Ae^{-[(x-x_0)/a]^2}$. The values of the parameters used are summarized in Table 1.

In the first experiment, R1, the ridge is centered in the western half of the basin ($x_0 = -0.6$), it has a half-width $a = 0.2$ and its maximum height is $A = 1.5$. The experiment was integrated in time until the steady state state was reached. The prediction of the analytical solutions is that the lower layer should move only in the region of "closed contours" (the region where no contours are drawn in Fig. 1a) and it should be at rest in the region of "blocked contours" (the region where the lower layer potential vorticity contours trace back to the southern, northern or eastern boundary). A strong jet should be observed along the characteristic marked by a thick line in Fig. 1b. In Figs. 2a, b the stream-

TABLE 1. Summary of the parameters used for the experiments in the presence of a ridge-like topography of the form $hb = Ae^{-[(x-x_0)/a]^2}$ and of an Ekman pumping of the form $g(x, y) = -\cos(\pi y/2)$. All the quantities are nondimensional. In the definition of the maximum Reynolds number, ψ_{2max} is the maximum value of ψ_2 in the interior, excluding the recirculation gyre.

Experiment	A	a	x_0	γ	κ	δ	$F_1 = F_2$	ψ_{2max}/κ
R1	1.5	0.2	−0.6	0.0005	0.018	0.009	4	44
R2	1.5	0.2	0.0	0.0005	0.025	0.0125	6	34
R3	1.5	0.2	0.0	0.0005	0.050	0.025	6	17

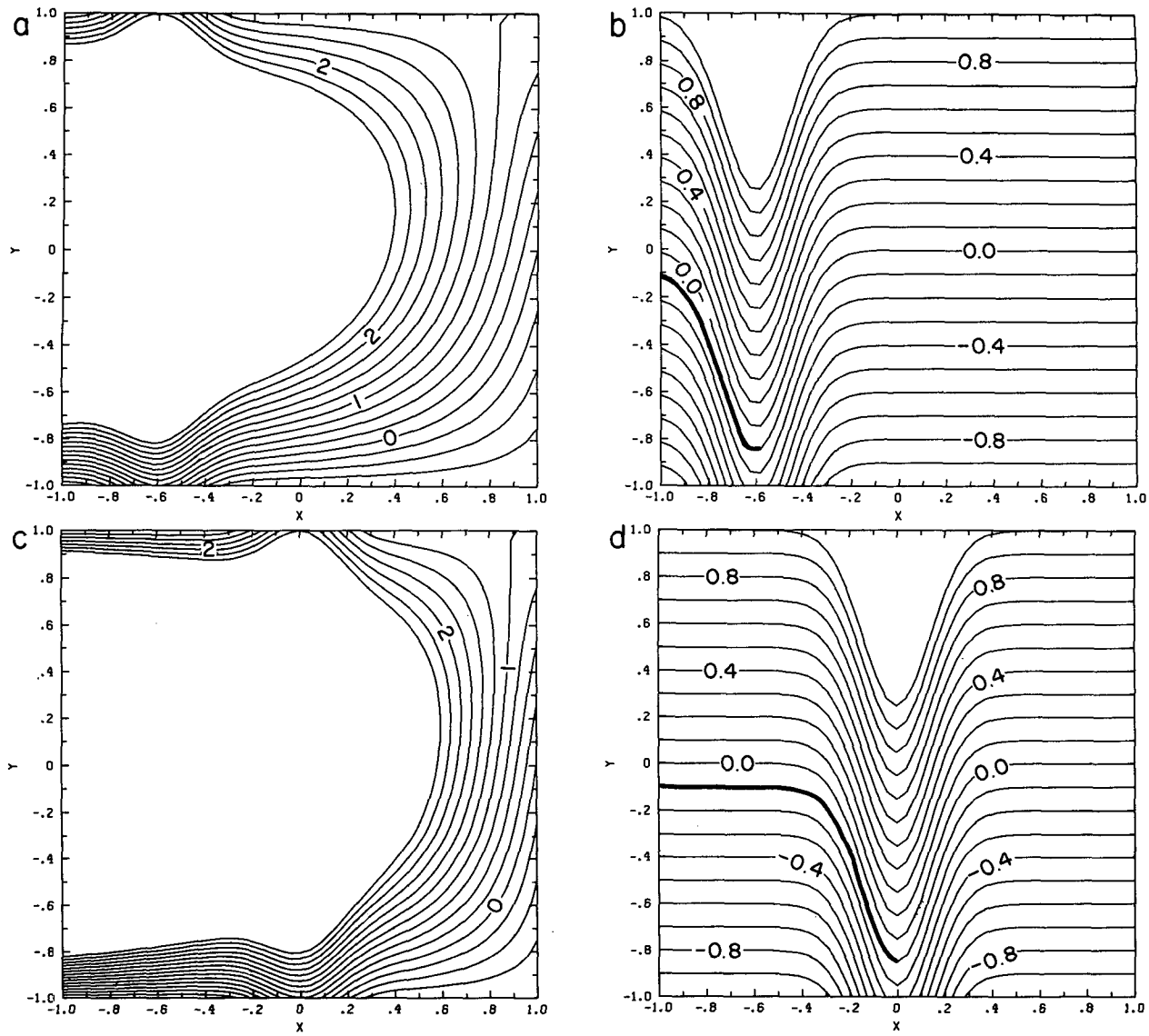

FIG. 1. (a) Lower-layer potential vorticity contours, as predicted by the inviscid solution, for the parameters used in R1. The abyssal flow should be confined in the region where no contours are drawn ("closed contour"), and $q_2 - \delta/\kappa\psi_2$ should be constant there. (b) Contours of $\xi = y + hb/2$ for the parameters used in R1. According to the inviscid solution, in the "closed contours" region, the geostrophic contours for the upper layer flow are parallel to ξ. The internal jet should be observed along the thick line. (c) As in (a) but for the parameters used in R2. (d) As (b) but for the parameters used in R2.

function fields are shown and indeed a crowding of the streamlines can be observed near the region of the dividing characteristic, although the flow intensification appears along a characteristic ξ different than that indicated in Fig. 1b. The reason for this discrepancy is that there is some viscously driven lower layer flow outside the region of "closed contours". The formula obtained in CP for the vertically integrated difference in transport across the dividing characteristic is, in the present nondimensional units,

$$T = A(F_2^{-1} - x_0 - a/2 + 1)/2. \qquad (3.1)$$

Equation (3.1) is valid for a simple piecewise continuous topography of the form:

$$h = \begin{cases} -A|x - x_0|/a + A, & \text{for } |x - x_0| < a \\ 0, & \text{for } |x - x_0| > a \end{cases}$$

where A is the maximum height of the ridge, x_0 is the center of the ridge and a is the halfwidth of the ridge, and for piecewise continuous Ekman pumping of the form

$$g(x, y) = \begin{cases} y - 1, & \text{if } y > 0 \\ -y - 1, & \text{if } y < 0 \end{cases}$$

Although the form of the topography and of the Ekman pumping used in the numerical experiments are a

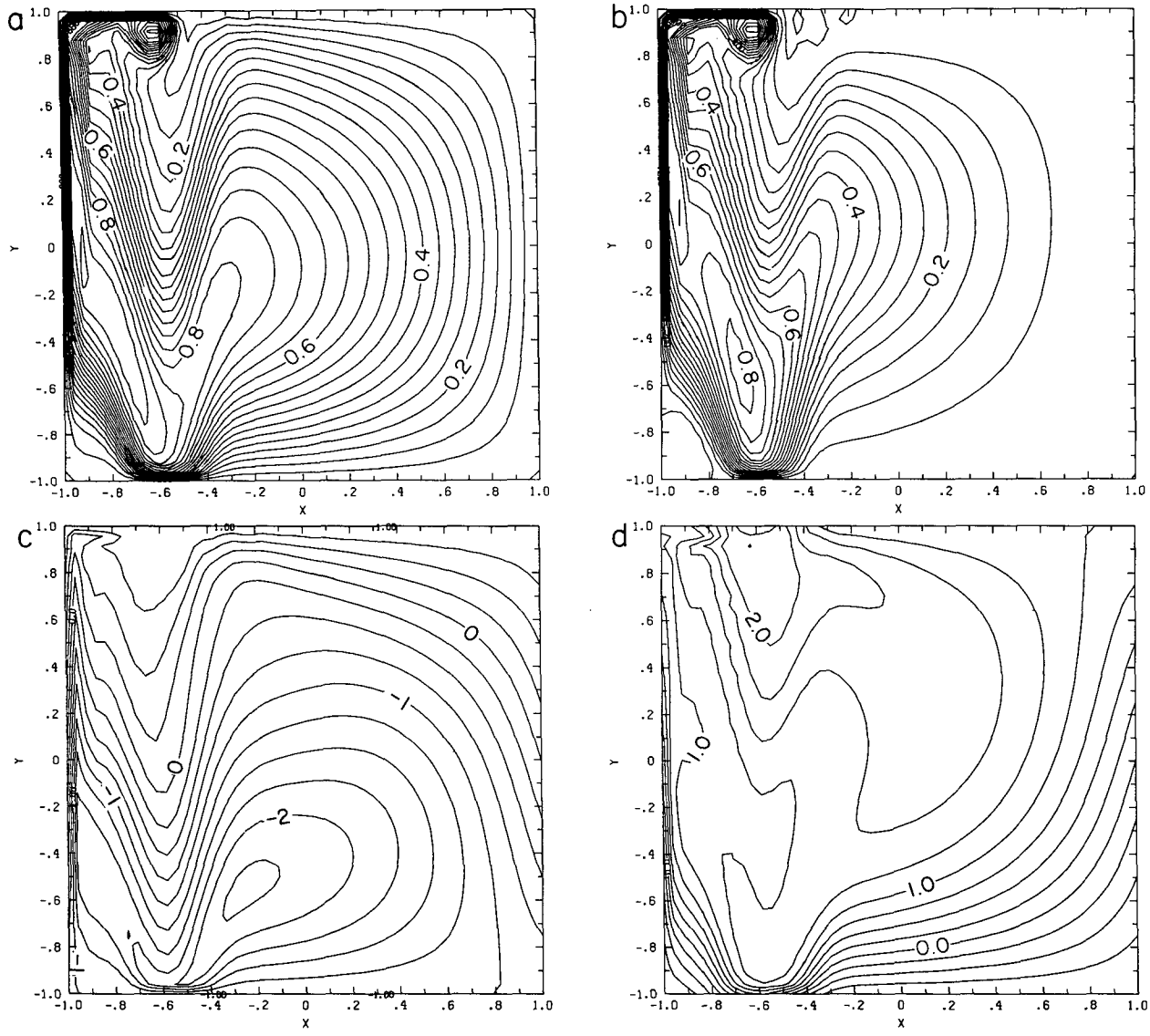

FIG. 2. Streamfunction and potential vorticity fields for the experiment R1. (a) Upper layer streamfunction. (b) Lower layer streamfunction. (c) Upper layer potential vorticity. (d) Lower layer potential vorticity. Notice the strong flow intensification occurring along the contour $\xi = -0.4$ of Fig. 1b. At the same location neither potential vorticity field exhibits a gradient enhancement.

smoothed version of those used in the analytical model, there is a quantitative similarity and I will compare (3.1) to the numerical results.

Because the thickness of the internal boundary layer in the numerical experiment is finite, the choice of the streamfunction values on each side of the dividing characteristic is to some extent arbitrary. My choice from inspection of Fig. 2 is $\Delta\psi_1 = 0.80$ and $\Delta\psi_2 = 0.75$, so that the vertically integrated jump is $T = 1.55$. For the values of the parameters used in this experiment, (3.1) gives $T = 1.31$, which is in good agreement with the numerical results. In Fig. 2c, d the potential vorticity fields are shown for the experiment R1. The lower layer potential vorticity gradients are greatly reduced in the region of closed contours, where the bulk of the abyssal flow occurs, with respect to the region of "blocked" contours (comparison should be made with the potential vorticity contours of the upper layer in the same region). Notice that, in agreement with the theoretical prediction, there is no enhancement of the potential vorticity gradients in the region where the jump in the streamfunction fields occur. As remarked in CP, this is because the jump in transport is depth independent and thus does not contribute to the vortex stretching term in the potential vorticity field. Relative vorticity gives a small contribution to the total vorticity field, except in the northwest corner where a recirculating gyre appears.

Another prediction of the analytical solution is that in the region west of the ridge the jet continues to flow zonally until it impinges upon the solid western boundary. In the experiment just discussed the ridge is so close to the western boundary of the basin that this effect cannot be revealed.

In the second experiment, R2, I moved the center of the ridge eastward, to the center of the basin, so that $x_0 = 0$. The height was kept the same, $A = 1.5$, and so was the halfwidth, $a = 0.2$. The other parameters are listed in Table 1. Notice that F_1 and F_2 have been increased in this experiment weakening the stratification and making the flow more vertically coherent. The experiment was integrated in time from rest until steady state was reached. The abyssal flow should be confined within the "closed contour" region (the blank region in Fig. 1c) and a strong jet should be observed along the characteristic ξ marked by a thick line in Fig. 1d. The streamfunction and potential vorticity fields are shown in Fig. 3. Again a strong intensification of the gradients occurs in the streamfunction fields (Fig. 3a, b), but not in the potential vorticity fields (Fig. 3c, d) at the location of a more southern characteristic than that predicted by the inviscid calculation (the thick line in Fig. 1d). The inviscid limit theory predicts that the vertically integrated difference in transport across

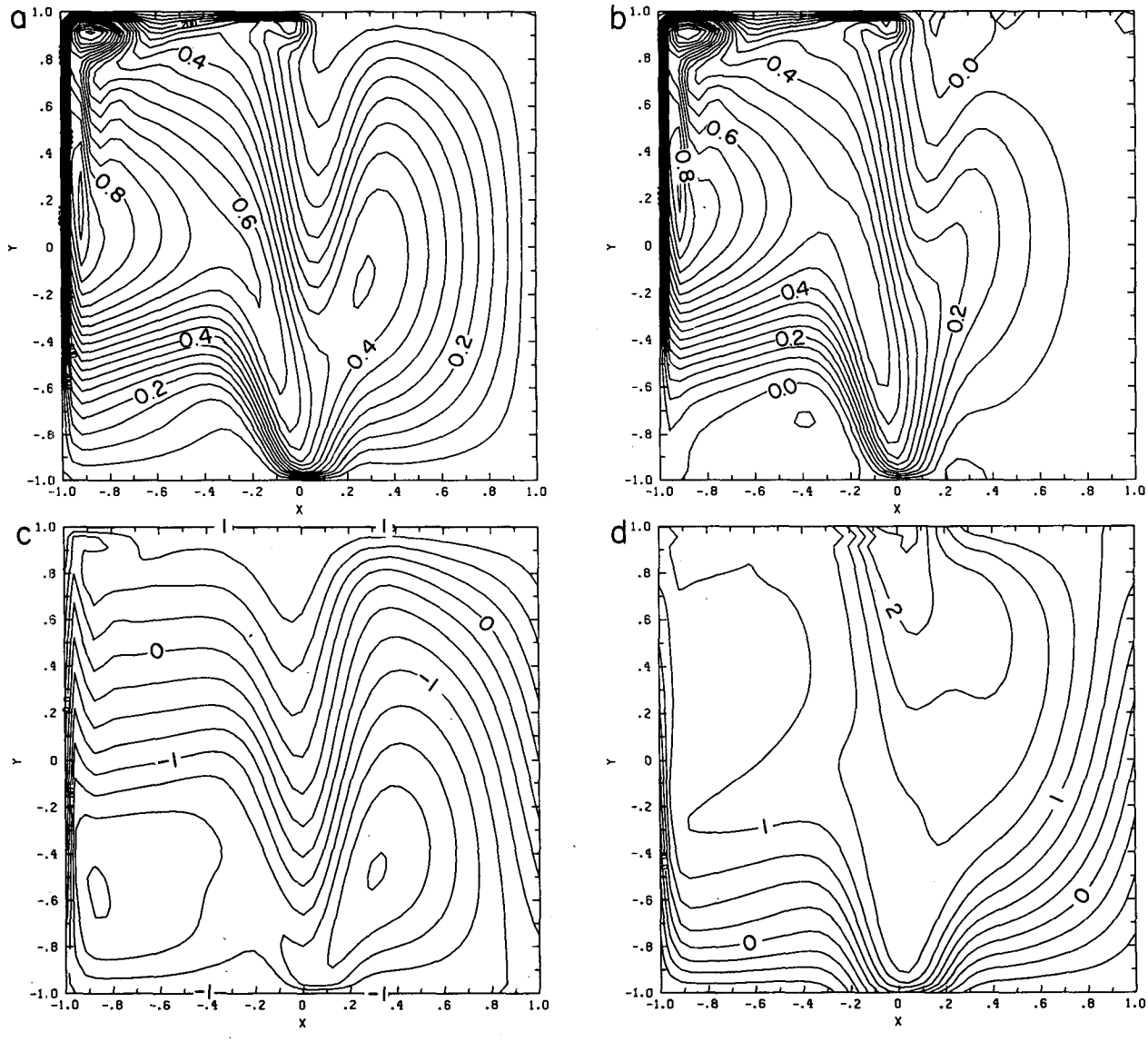

FIG. 3. Streamfunction and potential vorticity fields for the experiment R2. (a) Upper layer streamfunction. (b) Lower layer streamfunction. (c) Upper layer potential vorticity. (d) Lower layer potential vorticity. Notice the strong flow intensification occurring along the contour $\xi = -0.4$ of Fig. 1b. At the same location neither potential vorticity field exhibits a gradient enhancement. The jump in transport across the dividing characteristic is smaller than that occurring in R1 because the ridge center has been moved westward.

the jet is, from (3.1), $T = 0.77$, in rough agreement with the numerical results, which give a value between 0.8 and 0.9. In the region west of the ridge ($x \leq -0.3$), the jet flows almost zonally westward until the western boundary is encountered.

In the last experiment, R3, I tried to assess the effects of diffusion, by keeping all the parameters the same as in R2 except for the diffusive terms, κ and δ, which were both increased by a factor of 2. The results are shown in Fig. 4 and they should be compared to those shown in Fig. 3. As expected the maximum amplitude of the flow is smaller in both layers for the more diffusive experiment. A remarkable feature is that the recirculating gyre, which occurred in the northwest corner of the basin in Fig. 3 has disappeared and only a mild overshooting of the western boundary current is observed. On the other hand, the flow just west of the ridge has become *larger* at the expenses of the flow east of the ridge, in the more diffusive experiment R3, thus enhancing the difference in transport T across the jet. This result suggests that diffusion is responsible for T being larger in the numerical experiments than in the analytic solution.

Although an increase by a factor of two in the diffusive terms produces some qualitative changes in the overall flow, the analysis of the viscous boundary layer

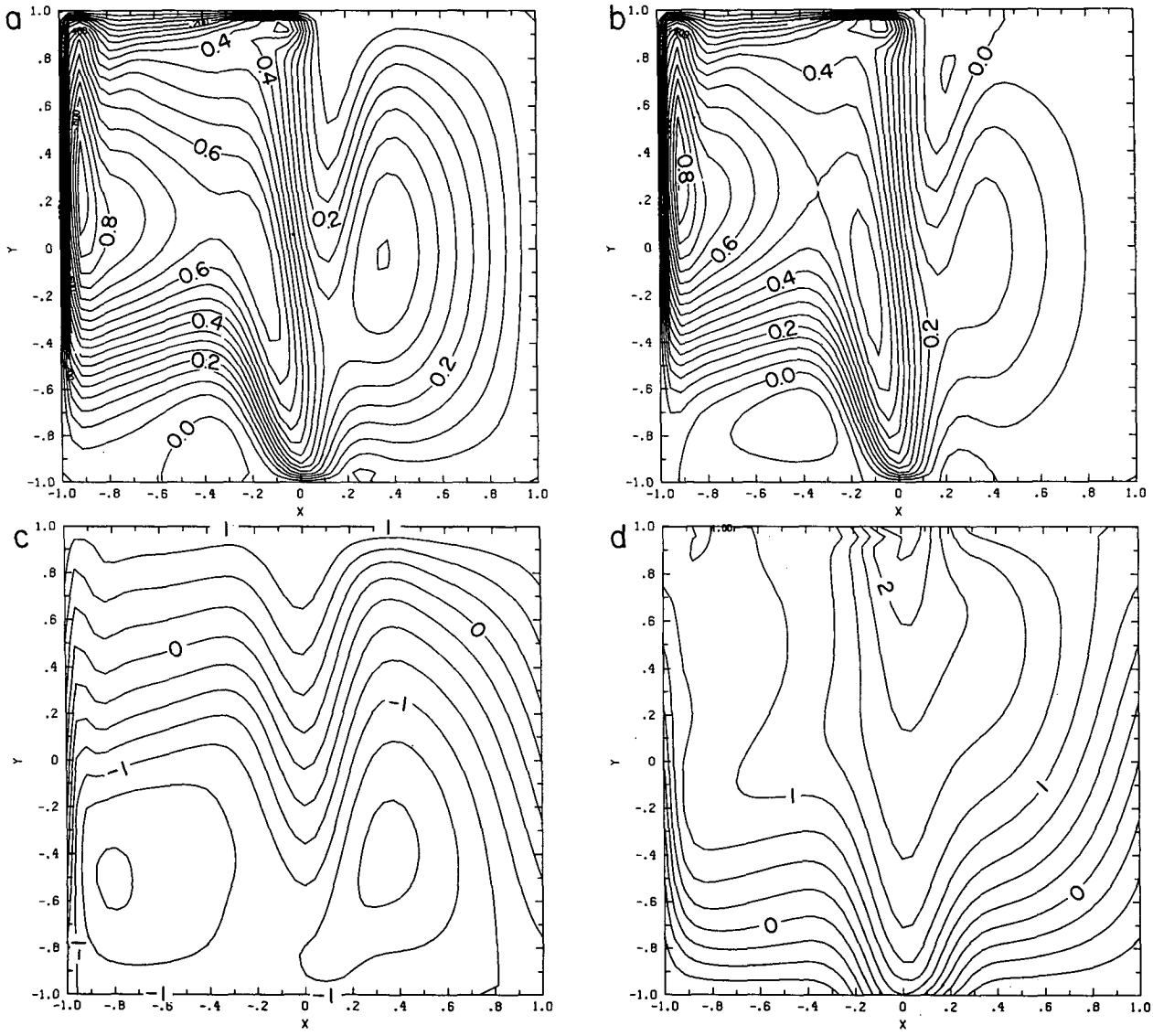

FIG. 4. Streamfunction and potential vorticity fields for the experiment R3. (a) Upper layer streamfunction. (b) Lower layer streamfunction. (c) Upper layer potential vorticity. (d) Lower layer potential vorticity. An increase by a factor of two in the diffusive terms brings some qualitative changes in the flow pattern: the recirculating gyre appearing in the northwest corner of the basin in Fig. 3 has practically disappeared. The internal boundary layer carries a larger transport and its width grows very slowly with diffusion.

for the vertically integrated flow shows that the jet expands very slowly as diffusion is increased. Defining $\psi = \psi_1 + \psi_2$, the potential vorticity equation for the barotropic flow is

$$J(\psi, y + h/2) + \gamma[J(\psi_1, \nabla^2\psi_1) + J(\psi_2, \nabla^2\psi_2)] = g(x, y) + h_x/(2F_1) + \kappa\gamma\nabla^4\psi - \delta\nabla^2\psi/2.$$

The property that $q_2 = \delta\psi_2/\kappa + \text{const}$ has been used and terms of order $\delta/(\kappa F_2)$ have been neglected. Simple scaling analysis shows that the dominant balance for the barotropic flow in the region of the jump is given by

$$J(\psi, y + h/2) = \gamma\kappa\nabla^4\psi - \delta\nabla^2\psi/2 \quad (3.2)$$

where both dissipative terms are kept because, for the values of the parameters used, $(\delta/2)^{1/2} \approx (\kappa\gamma)^{1/4}$. It turns out that for the experiment R2 lateral diffusion of potential vorticity is bigger than bottom friction, so that the boundary layer width is $O[(\kappa\gamma)^{1/4}]$, and the second term of the right hand side of (3.2) is subdominant. In the experiment R3 the two terms on the right hand side of (3.2) are of the same order, suggesting that for different values of the parameters the dominant balance may be different, and the boundary layer width may grow as $(\delta)^{1/2}$.

In all the experiments presented so far diffusion is quite large and we are quite far from the asymptotic regime discussed in the analytic solutions of CP. Indeed the flow in the "blocked" region is substantial and potential vorticity is not very well homogenized in the lower layer. Nevertheless the establishment of an internal jet induced by the ridge-like topography is undeniable even in the experiment R3 where the maximum Reynolds number $\psi_{2\max}/\kappa$ is as low as 17. The numerical experiments thus confirm that, in the presence of bottom topography of varying slope, strong boundary layers are formed in the interior of the ocean. For the moderate values of diffusion used here, the internal jets do not produce instabilities, and a steady state is possible. In summary, the occurrence of these strong jets is not affected by the inclusion of diffusion and inertial effects, which simply smooth the jump in transport over a finite width, which grows slowly as diffusion is increased.

4. Constant slope topography

In CP we showed that, in the presence of bottom topography which depends linearly on longitude, strong jets were generated at the boundary of the region of abyssal flow, and this region is well inside the interior of the basin. In the inviscid limit the internal jets arise because in the region of abyssal motion where q_2 is constant, the flow is governed by

$$(1 + H_1/H_2)\psi_{2x} - h_x\psi_{2y} = g(x, y) + h_x/F_1 \quad (4.1)$$

with $\psi_2 = 0$ on the boundary of closed q_2-contours region. Equation (4.1) is a partial differential equation with characteristics

$$\xi = y + H_2h/(H_2 + H_1). \quad (4.2)$$

As shown in CP, in general the characteristics (4.2) intersect twice the outermost closed q_2 contour in the interior, and thus the matching with the motionless "blocked region" cannot be satisfied on both sides of the boundary. In CP there is the implicit presumption that the flow mismatch can be smoothed over a diffusive boundary layer. Notice that, unlike the mismatch occurring in the presence of a topographic ridge, the flow mismatch just described does not arise in a barotropic model.

A series of experiments were carried out in order to reproduce the occurrence of the internal jets described in CP. A detailed account of the numerical experiments can be found in Cessi (1987). In the following I will analyze one experiment only, which is representative of the results obtained, and is also the most inviscid case I could carry out with the given resolution.

In the experiment presented I forced the top layer with the same Ekman pumping used in the previous section, i.e., $g(x, y) = -\cos(\pi y/2)$, but the bottom topography is of the form $hb = -\alpha x$, with $\alpha > 0$. The values of the parameters used are summarized in Table 2. The inviscid calculation predicts that the lower layer should be in motion only in the region of "closed contours" (the empty region in Fig. 5), and that an internal boundary layer should be observed at the location marked by a thick solid segment in Fig. 5. The streamfunction and potential vorticity fields resulting after time integration from rest are shown in Fig. 6.

No sign of velocity intensification is evident in the streamfunction field except in the western boundary layer and in the recirculation region (northwest corner). The potential vorticity contours in the lower layer are quite different than those predicted by the inviscid calculation (Fig. 5), the difference being larger near the outermost closed q_2 contour. To assess the effects of diffusion I calculated the viscously driven abyssal flow in the "blocked contour" region. In this region the lower layer flow is weak and to first order the upper layer flow is in Sverdrup balance in the interior, while the lower layer is forced by the weak stresses induced by the upper layer motion

TABLE 2. Summary of the parameters used for the experiment in the presence of a constant slope topography of the form $hb = -\alpha x$ and of an Ekman pumping of the form $g(x, y) = -\cos(\pi y/2)$. All the quantities are nondimensional. In the definition of the maximum Reynolds number $\psi_{2\max}$ is the maximum value of ψ_2 in the interior, excluding the recirculation gyre.

Experiment	α	γ	κ	δ	$F_1 = F_2$	$\psi_{2\max}/\kappa$
S2	0.8	0.0005	0.018	0.009	2	44

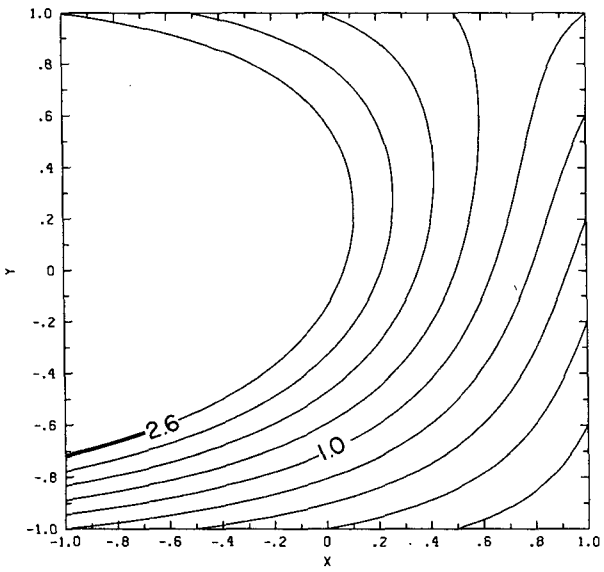

FIG. 5. Lower layer potential vorticity contours, as predicted by the inviscid calculation, for the parameters used in S2. The abyssal flow should be confined in the region where no contours are drawn ("closed contours"), and $q_2 - \delta/\kappa\psi_2$ should be constant there. The internal jets should be observed along the thick curve segments.

$$J(\psi_1, y) = -\cos(\pi y/2)$$

$$J(\psi_2, y + h + F_2\psi_1) = \kappa\nabla^2 q_2 \approx \kappa F_2 \nabla^2 \psi_1 \quad (4.3)$$

with boundary conditions $\psi_2 = 0$ on $x = 1, y = 1$. This simple set of linear equations was solved analytically, by first solving (4.3a) and then integrating (4.3b) along the characteristics shown in Fig. 5. The integral expression thus obtained for ψ_2 was calculated numerically using an IMSL routine. The lower-layer flow resulting from the solution of this linear problem is shown in Fig. 7a. The viscously driven flow is indeed largest in the region where the topographically induced jet should be observed. The amplitude, though, is about a factor of five smaller than that observed in the numerical experiment. The reason for this discrepancy is that in the linear calculation (4.3) the strong recirculating gyre occurring in the northwest corner of the basin has not been modeled. Specifically the contribution of the recirculating gyre to the source term ($\kappa\nabla^2 q_2$) in (4.3) is substantial as shown in Fig. 7b. Because the q_2 contours close to the region where the jet should be observed (contours $2.0 \leq q_2 \leq 2.6$ in Fig. 5) trace back to the northwest corner of the basin, crossing the "wake" of the recirculation, this localized source affects the whole region near the outermost closed q_2 contour.

The presence of the viscously driven flow in turn deforms the lower layer potential vorticity contours in the interior so that they become parallel to the characteristics given in (4.2), thus avoiding the jump in transport described in CP. The reason why a moderate amount of friction and inertia has such a devastating effect on the prediction of the inviscid calculation is the following. In the inviscid theory it is crucial that the characteristics (4.2) intersect the boundary of the abyssal flow twice in the interior. If the distance between the two points of intersection is small the jump in transport will be small. Inspection of Fig. 5 shows that it is enough to deform the outermost closed q_2 contour by a small amount to avoid the abovementioned intersection.

I should point out that the experiment just discussed is the most inviscid I could obtain with the given resolution. At lower diffusivities strong instabilities, generated by the recirculating gyre appearing in the northwest corner of Fig. 6a, b rendered the problem numerically intractable.

In summary, the numerical experiments aimed at reproducing the occurrence of the internal jets in the presence of constant slope topography, described in CP, produced results that were not in agreement with the theory developed by CP. The reason for this disagreement is twofold: on one hand the same diffusive interfacial stresses responsible for the motion in the abyssal region renders the flow more vertically coherent than it would be in the inviscid limit. Thus phenomena that rely heavily on baroclinicity are discouraged. On the other hand, reduction of diffusion leads to the onset of a recirculating inertial gyre (with strength that increases as diffusion is decreased) and this acts as a localized source of potential vorticity for the abyssal flow. Because of this source the region of abyssal motion is larger than that predicted by the calculations obtained for the inviscid limit, and the characteristics (4.2) do not intersect the outermost closed q_2 contours twice in the interior, and the need for internal boundary layers is avoided.

A solution of the inviscid problem, an alternative to that presented in CP, has been proposed by de Szoeke (1985). In de Szoeke's proposed pattern the flow in the upper layer is not closed, and thus does not satisfy the no normal flow condition on the eastern wall. Unfortunately the circulation patterns of the experiments that I performed do not agree with de Szoeke's prediction either.

5. Summary and discussion

In CP it has been shown that, in the presence of x-dependent topography, strong internal boundary layers are found when diffusive and inertial effects are neglected. Two types of jets were discussed. One occurs in the presence of topography of varying slope and arises both in vertically homogeneous and stratified models. The other occurs even in the presence of constant slope topography as long as the bottom elevation depends on longitude. The latter internal boundary layer is found only in baroclinic gyres, although it has a component which is depth independent.

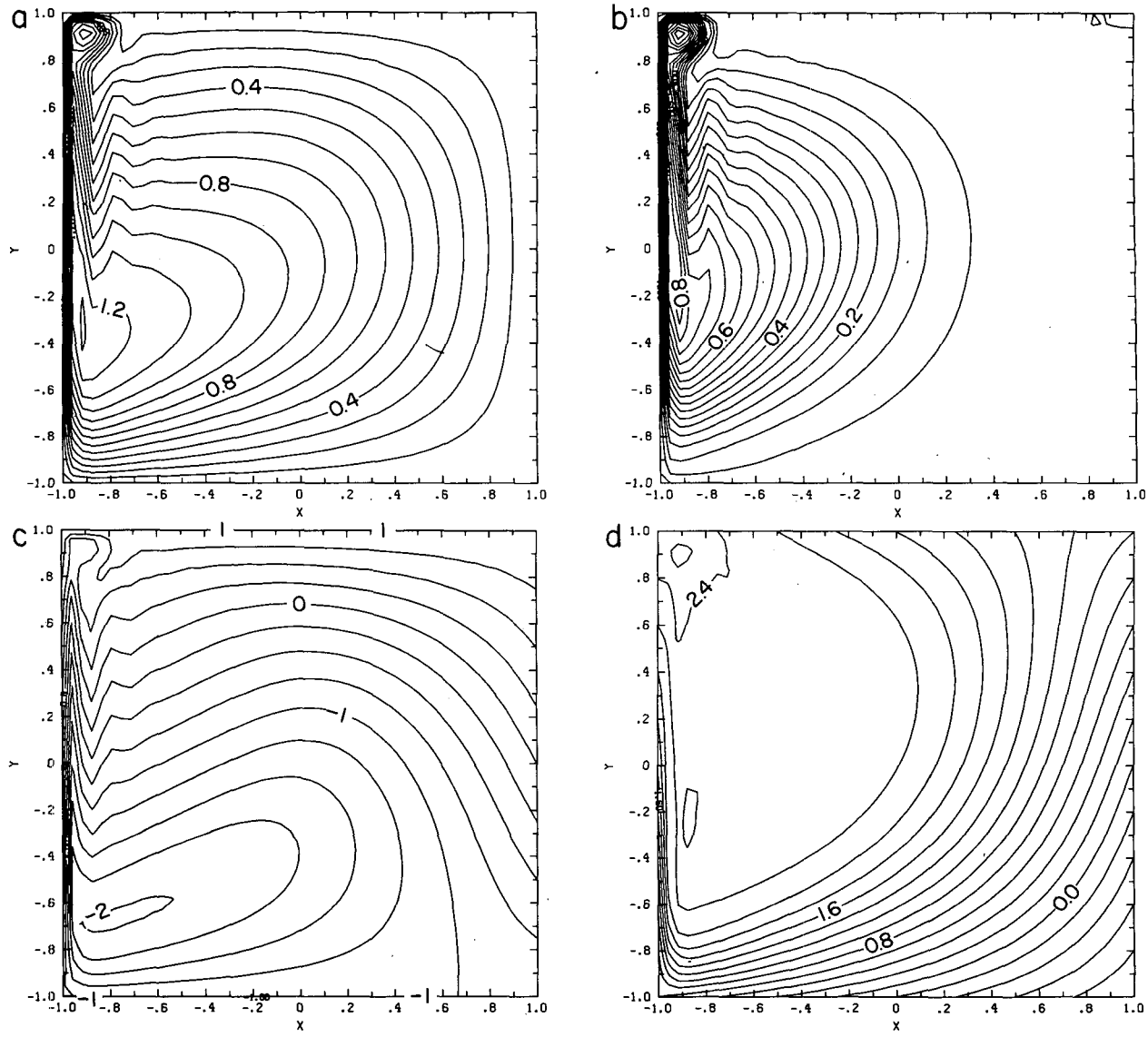

FIG. 6. Streamfunction and potential vorticity fields for the experiment S2. (a) Upper layer streamfunction. (b) Lower layer streamfunction. (c) Upper layer potential vorticity. (d) Lower layer potential vorticity. The lower layer moves also in the "blocked" region avoiding the onset of an internal boundary layer. The q_2 field is quite different from that shown in Fig. 5. For example the contour $q_2 = 2.4$ has moved from the "blocked" region to the "closed" region.

In order to test the robustness of the results I included the effects of lateral and interfacial friction as well as of inertia. The problem was solved numerically by time integration until the steady state was reached. The internal jets, connecting the southern to the western boundary layers in the presence of a ridge-like topography, found in the numerical model agreed with the results of the inviscid theory. Consistent with the inviscid prediction, the potential vorticity field does not exhibit the increase in gradient observed in the streamfunction field at the jet location. The vertically integrated transport carried by the jets was found to be in quantitative agreement with the analytical solution. The occurrence of the internal boundary layer was shown to survive moderate increases in the diffusion coefficient and the jet width grows very slowly when κ is increased. This indicates that the inviscid result survives to the inclusion of weak nonconservative effects.

The question that remains open is why, although a large ridge is present in the North Atlantic, the internal jets discussed here and in CP are not observed. A straightforward reason could be ascribed to the fact that the ocean is actually deeper than it has been assumed in the previous calculations and that the wind driven circulation does not penetrate all the way to the bottom. This is the case considered by Verron et al.

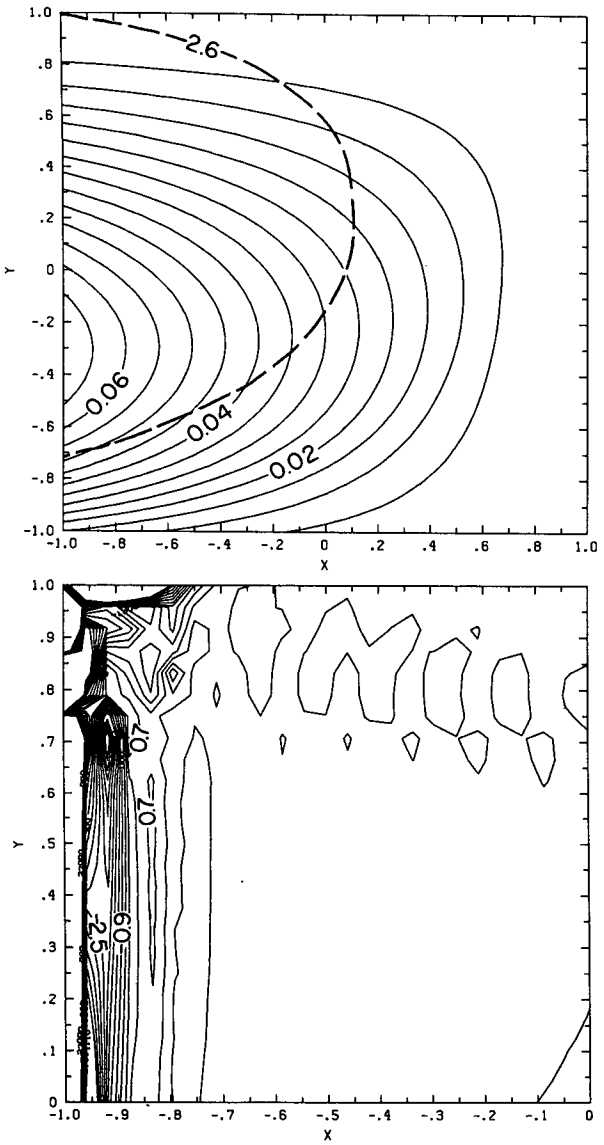

FIG. 7. (a) Viscously driven lower layer flow resulting from the solution of (4.3b) for the parameters used in S2. The streamlines to the west of the dashed line (outermost closed q_2 contour) are meaningless, because they are in the region of closed q_2 contours. The amplitude of the solution is too small. (b) Contours of $\kappa\nabla^2 q_2$ in the northwest half of the basin (contours of $|\kappa\nabla^2 q_2| \geq 4$ have been removed). In the recirculation region $\kappa\nabla^2 q_2$ is very large and this region extends eastward in the interior.

(1987) who analyzed the results of a wind driven, quasi-geostrophic two layer model in the presence of a shallow Mid-Atlantic ridge. In their model the lower layer circulation is confined to the recirculation region west of the ridge axis (all the potential vorticity contours are "blocked"), and there is no interior flow. However, because the Mid-Atlantic ridge is very high, it is conceivable that it penetrates the wind driven gyre. In any case the bottom waters are set in motion by the upwelling due to the thermohaline circulation as in the case analyzed by Welander (1969), but the jets may be hard to detect due to the smallness of the deep flow.

Another, more subtle explanation for the abscence of the internal jets, described in section 3, may be found in the actual geometry of the Mid-Atlantic ridge. First, note that the southern boundary placed in the model basin is not essential to the occurrence of the internal jets. The same phenomenon would arise if the ridge was confined in the meridional direction as well as in the x-direction, as in Verron et al.'s model. In that case the jet would flow *around* the southern edge of the ridge and then continue northward and westward as in the cases presented in Figs. 2, 3 and 4. In the North Atlantic the southern edge of the Mid-Atlantic ridge occurs in the equatorial region where the quasigeostrophic dynamics used here and in CP fail. This might be one of the reasons why the internal jets described here are not observed in the North Atlantic.

The numerical experiments, aimed at reproducing the baroclinic jets described by CP in the presence of constant slope topography, did not agree with the prediction of the inviscid theory. The discrepancy occurs because interfacial friction locks the two layers together making the flow vertically coherent. Therefore the effects that depend crucially on the baroclinicity of the flow are discouraged. This is also why, in the presence of ridge-like topography, the numerical results are in agreement with the inviscid calculation: the jets are present also in a vertically homogeneous model. Moreover, for small values of diffusion, an inertial recirculating gyre is generated and its size and strength increase as diffusion is decreased. Such a gyre, although confined in the Northwest corner of the basin, provides a source of potential vorticity for the abyssal flow which violates the assumption made in CP that the forcing in the abyssal layer is weak.

APPENDIX A

Description of the Numerical Model

Ierley's model solves the following quasigeostrophic, two-layer equations (in nondimensional form):

$$\frac{\partial q_1}{\partial t} + \epsilon J(\psi_1, q_1) = g(x, y) + \kappa\nabla^2 q_1$$

$$\frac{\partial q_2}{\partial t} + \epsilon J(\psi_2, q_2) = -\delta\nabla^2\psi_2 + \kappa\nabla^2 q_2$$

where

$$q_1 = \theta_1 + y = \gamma\nabla^2\psi_1 + F_1(\psi_2 - \psi_1) + y$$

$$q_2 = \theta_2 + y + h = \gamma\nabla^2\psi_2 + F_2(\psi_1 - \psi_2) + y + h$$

$$\epsilon = L_y/L_x \text{ (the aspect ratio of the basin)}$$

$$\nabla^2 = \epsilon^2\frac{\partial^2}{\partial x^2} + \frac{\partial^2}{\partial y^2}$$

with boundary conditions $\psi_1 = \psi_2 = \theta_1 = \theta_2 = 0$ on $x = \pm 1$, $y = \pm 1$.

Solutions are represented in the form:

$$\begin{pmatrix} \psi(x, y, t) \\ \theta(x, y, t) \end{pmatrix} = \sum_{i=0}^{48} \sum_{j=0}^{48} \begin{pmatrix} \Psi_{ij}(t) \\ \Theta_{ij}(t) \end{pmatrix} T_i(x) T_j(y)$$

where $T_n(s)$ are the Chebyshev polynomials of the first kind. The Θ_{ij} are time stepped with a Crank-Nicholson scheme, and the Ψ_{ij} are obtained by solving the Poisson and Helmholtz equations resulting from the barotropic and baroclinic streamfunction fields respectively. The diagonalization scheme, introduced by Haidvogel and Zang (1979), is used in the y direction for the Poisson/Helmholtz equations. The remaining problem of 49 coupled linear equations in x is solved reducing the equations to a quasi-tridiagonal form.

The Jacobian terms are calculated in real space, using a NCAR Cray matrix multiplication routine, and use is made of a Cray optimized fast Fourier transform.

The code contains a diagnostic routine which computes the integral of the diffusive vorticity flux over the whole basin. In the steady state one should find

$$\kappa \oint \nabla q_1 \cdot \mathbf{n} dl = -\int dA g(x, y)$$

$$\kappa \oint \nabla q_2 \cdot \mathbf{n} dl = \delta \oint \nabla \psi_2 \cdot \mathbf{n} dl$$

with the integrals performed over the whole basin. In all the experiments presented solutions were considered to have reached the steady state when

$$\kappa^{-1} \frac{\partial}{\partial t} \int dA q_1 = \oint \nabla q_1 \cdot \mathbf{n} dl + \int dA g(x, y) \Big/ \kappa \approx 10^{-2}$$

$$\kappa^{-1} \frac{\partial}{\partial t} \int dA q_2 = \oint \nabla q_2 \cdot \mathbf{n} dl - \delta \Big/ \kappa \oint \nabla \psi_2 \cdot \mathbf{n} dl \approx 10^{-2}.$$

Acknowledgments. I am indebted to Dr. G. R. Ierley for generously giving me his numerical model. I thank Joseph Pedlosky for numerous advices and suggestions. I was supported by NSF ATM84-13515. Partial support by NSF 8421074-OCE is also acknowledged. The numerical calculations were performed on computers located at NCAR*.

REFERENCES

Cessi, P., 1987: On the role of topography and of boundary forcing in the ocean circulation. Ph.D. thesis, MIT/WHOI Joint Program in Oceanography, 197 pp.

Cessi, P., and J. Pedlosky, 1986: On the role of topography in the ocean circulation. *J. Mar. Res.*, **44,** 445–471.

de Szoeke, R. A., 1985: Wind-driven midocean baroclinic gyres over topography; extension of the Sverdup relation. *J. Mar. Res.*, **43,** 793–824.

Haidvogel, D. B., and T. Zang, 1979: The accurate solution of Poisson equation by expansion in Chebyshev polynomials. *J. Comput. Phys.*, **30,** 167–180.

Holland, W. R., T. Keffer and P. B. Rhines, 1984: Dynamics of the oceanic general circulation: the potential vorticity field. *Nature,* **308,** 698–704.

Ierley, G. R., and W. R. Young, 1983: Can the western boundary layer affect the potential vorticity distribution in the Sverdrup interior of a wind gyre? *J. Phys. Oceanogr.*, **13,** 1753–1763.

Rhines, P. B., and W. R. Young, 1982: A theory of wind-driven circulation. Part I: Mid-ocean gyres. *J. Mar. Res.*, **40**(Suppl.), 559–596.

Verron, J., C. Le Provost and W. R. Holland, 1987: On the effects of a Midocean Ridge on the general circulation: numerical simulations with an eddy-resolved ocean model. *J. Phys. Oceanogr.*, **17,** 301–312.

Welander, P., 1969: Effects of planetary topography on the deep-sea circulation. *Deep-Sea Res.*, **16,** 369–391.

* The National Center for Atmospheric Research is supported by the National Science Foundation.